Self-Structured Conductive Filament Nanoheater for Chalcogenide Phase Transition

Byoung Kuk You, Myunghwan Byun, Seungjun Kim, and Keon Jae Lee*

Department of Materials Science and Engineering, Korea Advanced Institute of Science and Technology (KAIST), 291 Daehak-ro, Yuseong-gu, Daejeon 305-701, Republic of Korea

ABSTRACT $Ge_2Sb_2Te_5$-based phase-change memories (PCMs), which undergo fast and reversible switching between amorphous and crystalline structural transformation, are being utilized for nonvolatile data storage. However, a critical obstacle is the high programming current of the PCM cell, resulting from the limited pattern size of the optical lithography-based heater. Here, we suggest a facile and scalable strategy of utilizing self-structured conductive filament (CF) nanoheaters for Joule heating of chalcogenide materials. This CF nanoheater can replace the lithographical-patterned conventional resistor-type heater. The sub-10 nm contact area between the CF and the phase-change material achieves significant reduction of the reset current. In particular, the PCM cell with a single Ni filament nanoheater can be operated at an ultralow writing current of 20 μA. Finally, phase-transition behaviors through filament-type nanoheaters were directly observed by using transmission electron microscopy.

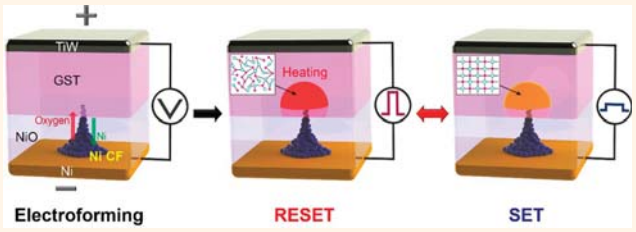

KEYWORDS: phase-change memory · low power consumption · conductive filament · nanoheater

Phase-change random access memories (PCRAMs) exploiting the dramatic difference of electrical resistance in a reversible phase transition of chalcogenide-based materials between amorphous (high-resistance) and crystalline (low-resistance) states have garnered huge interest for future data-storage generations.[1−13] Nonvolatile PCRAM is one of the strong candidates for a so-called "universal nonvolatile memory" to replace Si-based flash memory and volatile dynamic random access memory (DRAM) because of its outstanding advantages such as rapid write/erase speed, long write endurance, and high scalability.[4,7−9,13−18] In particular, phase-change memory (PCM) is approaching commercialization on the basis of mature technologies in the semiconductor industry.[19] However, there are a few unresolved problems that must be addressed to achieve high-density PCRAM devices, including high writing current for a crystal-to-amorphous phase change and cell-to-cell heat disturbance.[3−5,7,14,16,20,21] The most important issue is reducing the size of the contact area between the phase-change material and the heater electrode, which would be highly beneficial for reducing the reset current. Although scaling down is the most effective method for compatibility with the complementary metal-oxide semiconductor (CMOS) process, the resolution of conventional photolithography is restricted by the optical diffraction limit.[22,23] A few elegant approaches have been studied *via* nano-based methodologies such as nanowire/nanodot devices[3,24−27] and new structure design.[4,7] Nevertheless, effective solutions applicable to the conventional CMOS process have not been presented yet.

In this study, we present a method to achieve chalcogenide phase transition with self-structured nanoheaters of Ni conductive filaments (CFs) generated by electrical migrations of mobile oxygen vacancies.[28−30] The conductive filament phase-change memory (CF-PCM) devices were fabricated *via* three methods: TiW/GST depositions after the CFs' electroformation by contacting a Pt probe tip on NiO films (method 1, Figure 1), voltage sweeping to the top electrode (TE) after all film depositions without a Pt probe tip (method 2, Figure 2), and a single-filament growth using a conductive atomic force

* Address correspondence to keonlee@kaist.ac.kr.

Received for review April 29, 2015 and accepted June 3, 2015.

Published online June 03, 2015
10.1021/acsnano.5b02579

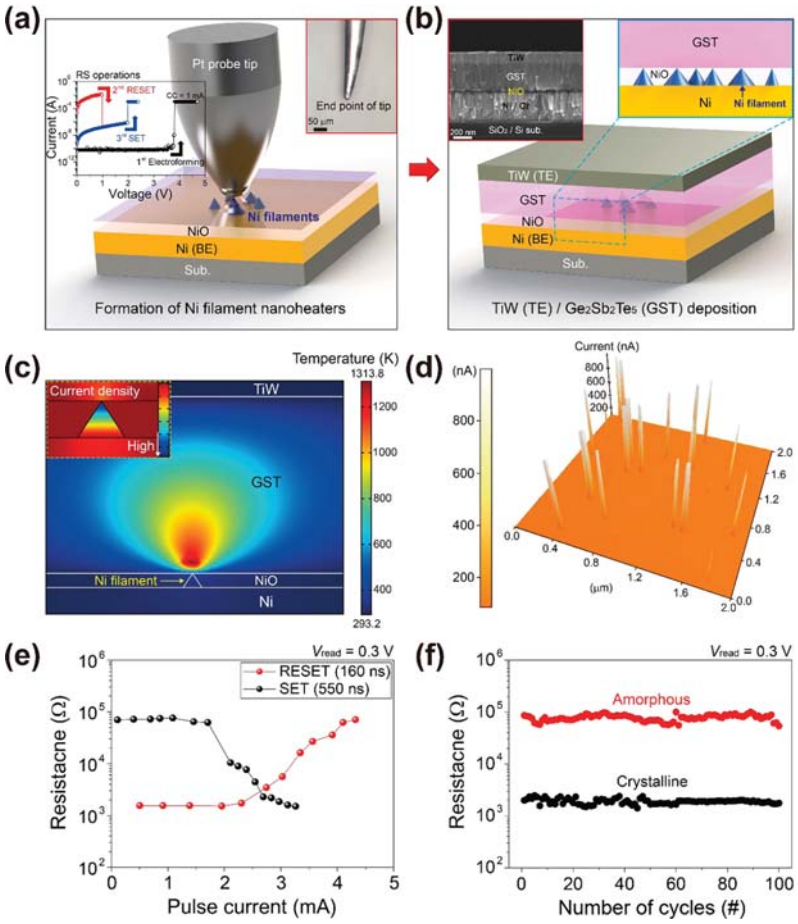

Figure 1. Formation of Ni filament nanoheaters by contacting a Pt-coated probe tip on NiO films and CF-PCM operation *via* Ni filament-induced heating. Schematics of the process for (a) Ni filament heater formation and (b) subsequent CF-PCM device fabrication. The left inset graph of panel a shows *I*−*V* curves of unipolar RS operations by using the Pt-coated probe tip on NiO/Ni films, and the right inset of panel a shows an optical image of the end point of the Pt-coated probe tip. The inset of b is the cross-section SEM image of the CF-PCM. (c) Temperature distributions of the CF-PCM device using an electrothermal simulation based on the FEM. The inset image shows the current density distributions of the CF-PCM cell. (d) CAFM results of the area where Ni filaments are formed (2 × 2 μm^2 scan area). (e) *R*−*I* curves of the CF-PCM device operated by a reset pulse width of 160 ns and a set pulse width of 550 ns. The reset and set current is 4.1 and 2.7 mA, respectively. (f) Writing endurance test during 100 cycles. The reading voltage for extraction of the resistance is 0.3 V.

microscopy (CAFM) tip (method 3, Figure 3). Both single- and multi-Ni filament nanoheaters achieved an ultralow power phase transition of PCM, highly concentrating the current density into the end point of the filament nanoheater. This approach can dramatically reduce the reset current of CF-PCM by 20 μA. The mechanism of nanofilament-induced heating was theoretically explained by electrothermal simulations based on the finite element method (FEM). The Ni CF was directly observed by employing transmission electron microscopy (TEM) in the amorphous NiO layer.[31] As a result, metallic cone-shaped Ni filaments have served as heaters with nanometer-scale vertices. This self-structured heater has a few-nanometer-sized contact area between the Ni CF and $Ge_2Sb_2Te_5$ (GST) films, significantly reducing the phase-change area. The reversible phase-change behavior of the amorphous-to-crystal state was microscopically observed by using TEM and energy dispersive spectrometer (EDS) elemental mapping.

RESULTS AND DISCUSSION

Phase-Transition Behaviors *via* Ni CFs Formed by Pt Probe Tip. Figure 1a schematically illustrates the formation of nanoscale Ni filaments into NiO films by using a Pt-coated probe tip under positive voltage (method 1). The end point of the Pt probe tip was approximately 15 μm in diameter, as shown in the right inset of Figure 1a. The left inset graph of Figure 1a demonstrates the current−voltage (*I*−*V*) curves of an electroforming process generating Ni CFs and subsequent reset/set operations corresponding with the reversible resistive switching (RS) of a typical unipolar resistive memory.[28−30,32] For such an electroforming process, oxygen vacancies move toward the base of NiO films, and simultaneously nickel ions are expected to move toward the tip surface, thus

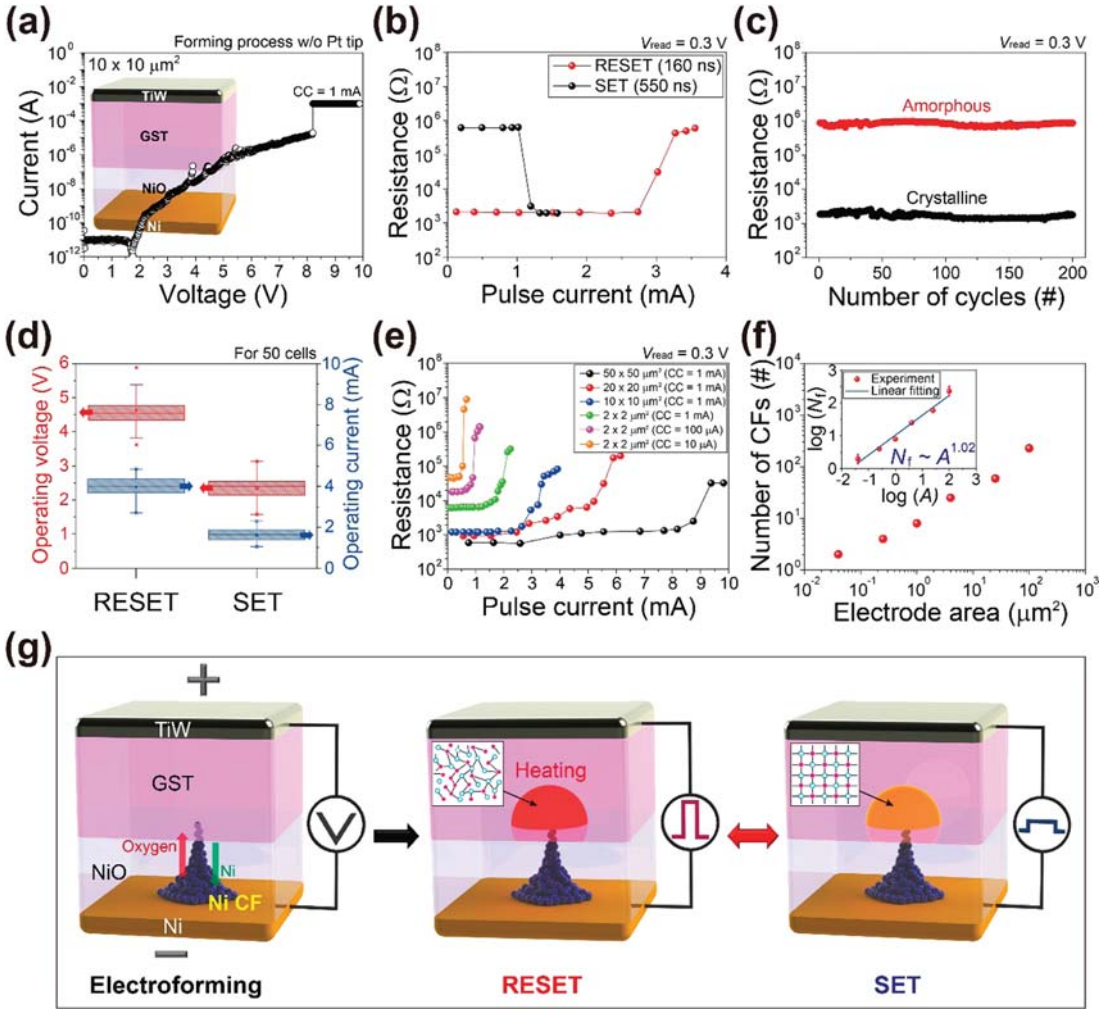

Figure 2. Electrical characteristics and operation mechanism of the CF-PCM devices without Ni CF formation by the Pt probe tip. (a) Electroforming *I*−*V* curve for filament growth of the TiW/GST/NiO/Ni CF-PCM device fabricated by successive film deposition. The electrode area is 10 × 10 μm^2, and the compliance current (CC) is 1 mA. (b) *R*−*I* curves of the CF-PCM device (I_{reset} = 3.2 mA and I_{set} = 1.1 mA). (c) Writing endurance test during 200 cycles. (d) Cell-to-cell statistical charts from operating voltages (red box) and currents (blue box). (e) Programming curves for crystalline to amorphous phase transition depending on the electrode area and CC. The CF-PCM device with an electrode area of 2 × 2 μm^2 operates at a reset current of 593 μA (CC = 10 μA). (f) Number of Ni CFs depending on the electrode area. The inset graph of panel f shows the relationship between filament number and electrode area. (g) CF-PCM operation mechanism *via* Ni nanofilament-induced heating. The Ni filament heater is grown through movements of both Ni vacancies and oxygen vacancies under the electrical voltage. After that, the reset/set pulse voltages result in the phase transition of the GST.

resulting in growth of nanosized Ni CFs, as demonstrated by the resistive memory device of the Pt/Ti/NiO/Ni structure (Supporting Information, Figure S1).[31] After the formation of Ni filament nanoheaters, the GST phase-change layer and the TiW TE were deposited to provide phase-transition behavior *via* self-structured CF nanoheaters (Figure 1b). A CF-PCM device having a cross-point structure over a 50 × 50 μm^2 area was fabricated on the Ni bottom electrode (BE). To provide the theoretical mechanism of the CF-induced heating of the GST material, electrothermal simulations were preferentially conducted by using the FEM. Figure 1c shows the temperature and current density distributions of the CF-PCM cell. We assumed that the contact size between the filament and the GST was 1 nm, and the applied current density (*J*) is 1.8 × 10^{10} A/m^2. The vertex of the Ni filament can shrink to the 1−2 nm through the electrical modification (Supporting Information, Figure S12). As shown in the inset image of Figure 1c, large current density was concentrated at the Ni filament. The highest current density was located at the vertex of the filament, resulting in the generation of Joule heating. The heat generated from the Ni filament heater induced a temperature increase of the GST layer over the melting point (888 K). The electrothermal simulation data were simply suggested in order to investigate the principle and trends of the CF-PCM device. The applied current density from simulation results and the measured current from real experimental data were not equal because the leakage current and heat losses from the

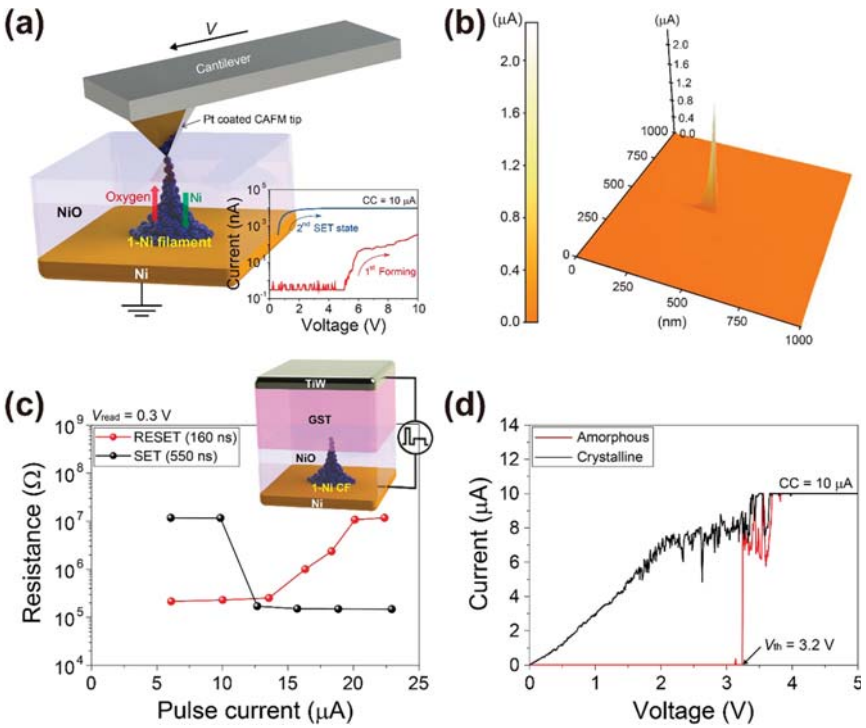

Figure 3. 1-Ni filament growth by using a Pt-coated CAFM tip and its CF-PCM device operations. (a) Schematic of the process of forming a 1-Ni filament nanoheater by contacting the Pt-coated CAFM tip (diameter = 20 nm) on NiO films. The inset graph of panel a shows the corresponding *I*−*V* curves during the electroforming process. (b) Current profile scanning on NiO films after the 1-Ni filament formation (tip bias = 0.5 V and scan area = 1 × 1 μm^2). (c) *R*−*I* curves and (d) *I*−*V* curves of the CF-PCM device with 1-Ni filament nanoheater (I_{reset} = 20 μA, I_{set} = 13 μA, and V_{th} = 3.2 V).

device structure were not considered in the FEM simulation. To clearly analyze the distributions of Ni CFs formed within the NiO layer, CAFM measurements were performed (Figure 1d and Figure S2). Current over 800 nA, directly measured on NiO films, was detected from localized nanoscale CFs. From the CAFM profile, the actual area contacted by a Pt probe tip was calculated to be about 123 μm^2 (slightly smaller than the probe tip area of ~177 μm^2). These conductive Ni filaments directly work as nanoheaters for the phase transition of the GST layer.

For electrical characteristics of the CF-PCM device, the BE was grounded and an electrical pulse was applied to the TE. First, a reset pulse of 160 ns width was applied to the TE, leading to a phase change of the GST from the crystalline to amorphous state. The reset current (I_{reset}) required for amorphization was measured to be 4.1 mA, and correspondingly the resistance increased by 2 orders (Figure 1e). It is noteworthy that the operation current in the present work is much lower compared to a conventional PCM device with a micrometer-sized contact area. Generally, a PCM with a 2-μm-diameter contact area between GST films and a TiN heater operates at 75 mA.[16] This significant reduction of the reset current indicates that our CF-PCM device works *via* Ni nanofilament heaters generated by the electroforming process. The set current (I_{set}) for the recrystallization of GST was measured to be 2.7 mA with a 550 ns pulse width. In addition, the *I*−*V* curves in Figure S3 show that the threshold voltage (V_{th}) is 1.1 V, which represents the phase-change behavior. These phase-change transitions were reversibly repeated during 100 cycles, as shown in the writing endurance test of Figure 1f. Unfortunately, this forming process of Ni CFs by the Pt probe tip induced large fluctuations of the operating voltage and current because the effective contact area between the NiO and the probe tip was not uniform in each fabrication process (Supporting Information, Figure S4).

CF-PCM Operation by Electroformed Filaments without the Pt Probe Tip. In order to provide a scalable fabrication process and reduce the cell-to-cell fluctuation, CF-PCM devices were fabricated by successive deposition of TiW/GST/NiO/Ni films without using the Pt probe tip (method 2). After the entire film deposition, the Ni BE was grounded and the TiW TE was applied by positive bias. Figure 2a shows the device structure with a 10 × 10 μm^2 electrode area and its corresponding electroforming *I*−*V* curves. Here, it should be noted that no filaments were grown at the initial state of the CF-PCM device. During the electroforming process under a sweeping voltage of 10 V to the TE, the Ni CFs were grown toward the anode and connected to the bottom of the GST layer. The Ni nanofilament heaters were restricted in the 10 × 10 μm^2 electrode area, and their sites were randomly distributed because

the electric fields were constant in the NiO layer.[31,33] Through this method, it is unnecessary to align the TiW/GST films onto the Ni CFs because the Ni filaments are grown beneath only patterned GST films. The reset/set current and threshold voltage were measured to be 3.2 mA/1.3 mA and 0.6 V, respectively, as shown in the resistance−current ($R-I$) and $I-V$ curves of Figure 2b and Figure S5a. This reset current of 3.2 mA (electrode area = 100 μm^2) is reasonable since the device fabricated in Figure 1 with an active electrode area of 123 μm^2 operates at a reset current of 4.1 mA. During 200 writing cycles, the CF-PCM device exhibited cyclic behavior of the reset/set switching without degradation of the resistance ratio and retained its two resistance states up to 10^4 s (Figure 2c and Figure S5b). In order to investigate the cell-to-cell uniformity, the electrical performance of 50 unit cells was measured under identical conditions (electrode area of 10×10 μm^2). Figure 2d shows the statistical charts from the operating voltage and current of 50 different cells, revealing markedly superior cell-to-cell uniformity compared to that of the CF-PCM devices operated by using a probe tip, as shown in Figure S4. The programming current for CF-PCM operations should be compared to that for the RS, strongly depending on whether or not the Ni CFs are ruptured. In our CF-PCM device, feasibility of reversible RS operation was confirmed after the repeated phase-change behaviors, as shown in Figure S6. The reset current required for transforming the phase-change material into an amorphous state was measured to be 3.2 mA, while the reset current for the rupture of the Ni filaments was measured to be over 8 mA, indicating that there was no substantial effect of the filament heaters during the CF-PCM operations. Although Joule heating for the reset operation of the CF-PCM cell results in a temperature increase of the GST layer above the melting point, the Ni filaments are not ruptured because the thermal conductivity of GST is much lower than that of nickel.[9] Most of the generated heat flows toward the GST films without raising the temperature at the end point of the Ni CFs (simulation results of Figure 1c). Nevertheless, when high enough current over the CF-PCM operation range is applied to the cell, the vertex of the Ni filaments may be ruptured as a consequence of oxygen diffusion into the Ni CFs.

It is generally acknowledged that the writing current of the PCM directly depends on the contact area between the phase-change material and the heater since the phase-change area decreases according to the down-scaling.[34] In contrast, here, two representative variables, the number and the thickness of Ni CFs formed in the NiO layer, should be reduced to shrink the reset current. The effective electrode area and the compliance current (CC) for the electroforming, therefore, should be controlled because the number and the thickness of filaments decrease with reduction of the electrode area and the CC, respectively. Figure 2e shows the programming data plots indicating different reset processes with variation of the electrode area and the CC. As the electrode area and the CC became smaller, the reset current for operating the device gradually decreased. In our CF-PCM device, the strong heat is generated by the high current density, resulting in the appropriate on/off ratio of an average of 2 orders. This resistance ratio was similar to that of GST-based PCM devices with nanostructures below 30 nm, which were previously reported.[3,7,21] It is evident that the reset current is proportional to the number of Ni CFs, because the filament number is directly related to the contact area between the filament heater and the GST films, as mentioned above. In addition, the thickness of the Ni filament has to be considered from the perspective of the contact area. Figure S7a and b show current density and temperature distributions of the CF-PCM cell with a thick Ni filament, corresponding to the electrical data related to the reset current depending on the CC, as shown in Figure 2e. We assumed that the contact size between the GST and the thick filament was 10 nm. A higher CC for electroforming induces the formation of thick Ni CFs, while a lower CC can make the filaments thinner. Under the same applied current density ($J = 1.8 \times 10^{10}$ A/m^2), the thin filament device has a smaller phase-change area and higher maximum temperature (1313.8 K, Figure 1c) than the thick filament device (1029.8 K, Figure S7 in the Supporting Information). These simulation results indicate that the thinner filament can effectively generate heat, decreasing the writing current. When the cell with a 2×2 μm^2 area and 10 μA CC was applied, the reset current of CF-PCM was measured to be 593 μA, approximately equivalent to that of the conventional PCM device operated at a 38 nm contact area.[9] In addition, comparative device dimensions in all CF-PCM cells of Figure 2e are shown in Table S1 of the Supporting Information. The corresponding power consumption calculated from the reset current/voltage was 1.77 mW (Supporting Information, Figure S8). Figure 2f presents the number of Ni filaments depending on the electrode area, which was obtained from the current scanning results *via* CAFM measurements (Supporting Information, Figure S2). We induced linear fitting of $N_f \approx A^{1.02}$ from a log−log scale plot, where N_f is the number of CFs and A is the electrode area. On the basis of this experimental observation, we strongly assume that scaling down of the electrode area would be effective for reducing the number of potential CFs in the contact area, thus making it possible to dramatically lower the reset current.

Operation Mechanism of CF-PCM. The detailed operating mechanism of the CF-PCM operated by Ni CFs is schematically described in Figure 2g. In the early stage of the filament electroformation, positively charged oxygen vacancies and negatively charged Ni vacancies

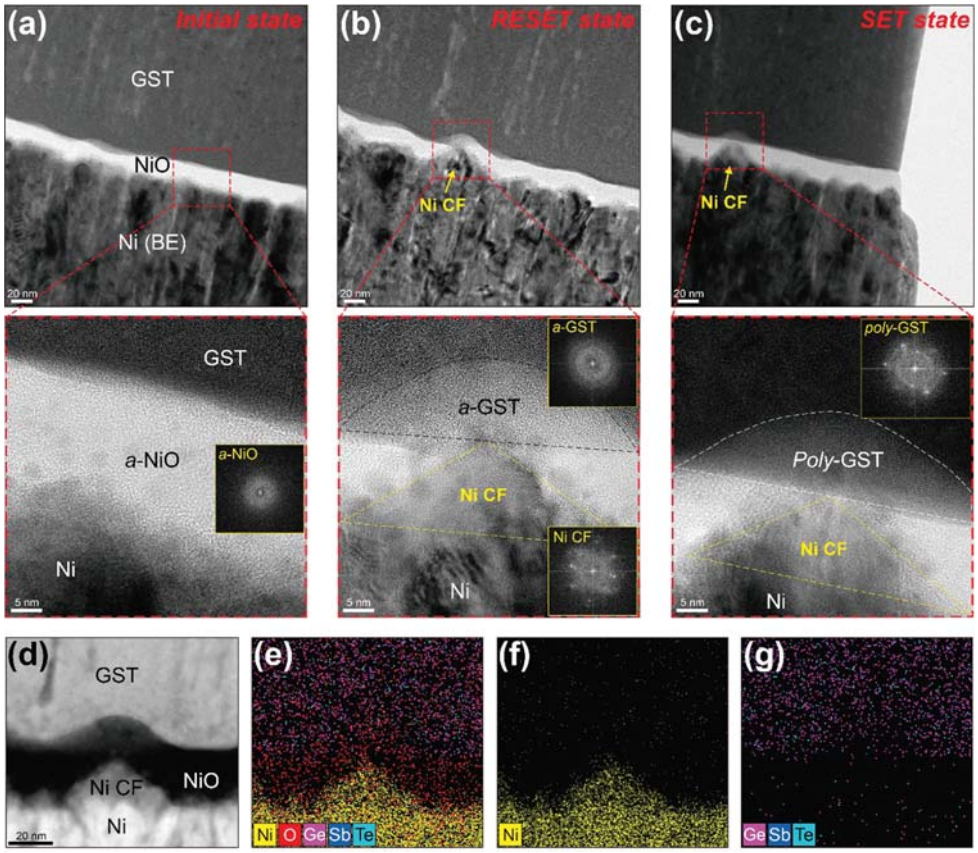

Figure 4. TEM analyses and EDS elemental mapping results of the CF-PCM devices with self-structured filament heaters. TEM images corresponding to the (a) initial state, (b) reset state, and (c) set state of the CF-PCM devices. The inset images of a–c show the FFT patterns for the crystallographic analyses of the phase-change region. (d) Bright-field TEM image of the reset state of the CF-PCM device. EDS elemental mapping results of (e) Ni, O, Ge, Sb, and Te, (f) Ni, and (g) Ge, Sb, and Te.

are expected to migrate toward the cathode and the anode, respectively, thus resulting in the formation of conductive Ni metallic filaments in the NiO films.[29,31,35] Once the filaments are formed, the reset current from a vertex of the Ni CF induces strong heating at the GST films, leading to amorphization of the contact region. During the reset process, the temperature of the contact area increases over the melting point of the GST material (888 K). When a set pulse is applied to the device, the contact area of the GST returns to the original crystalline state. The amplitude of the set pulse should be over the crystallization temperature but not higher than the melting temperature. These phase-transition behaviors are reversibly repeated during the reset/set switching.

CF-PCM with a Single Ni Filament Nanoheater. Diminishing the number of Ni filaments is beneficial in terms of power reduction of CF-PCM. For the formation of only one Ni filament, we employed the CAFM system with a Pt-coated AFM tip of 20 nm diameter (method 3). Figure 3a shows the single filament formation process by contacting the Pt-coated AFM tip onto the NiO films and simultaneously applying positive voltage to the cantilever (CC = 10 μA). A single Ni filament was grown toward the CAFM tip *via* migration of nickel and oxygen vacancies, and corresponding *I*–*V* curves are shown in the inset graph of Figure 3a. The single Ni filament heater was confirmed from the current scanning profile with a scan area of 1 × 1 μm^2 (Figure 3b). In this current scanning region, a more than 2 μA current peak was observed at only one location, which indicated the Ni CF grown into the NiO films. After the formation of the single Ni CF, GST and TiW films were deposited in consecutive order for the device fabrication. The CF-PCM with the single Ni filament was reversibly operated at an I_{reset}/I_{set} of 20 μA/13 μA, respectively (Figure 3c), and this ultralow programming current was also demonstrated from the *I*–*V* curves, as shown in Figure 3d. Furthermore, this ultralow power CF-PCM cell showed good reliability in both cycling endurance and the time retention test (Supporting Information, Figure S9). If the leakage current and heat losses from the microscale electrode were considered, a much smaller writing current would be expected. Therefore, further scaling-down of the cell size below 20 nm may lead to a dramatic decrease of the writing current to a few microamperes since only one Ni filament can be grown as a nanoheater to operate the CF-PCM device without using the CAFM tip. For these reasons, our CF-PCM process can be

incorporated with the sub-20 nm CMOS process of semiconductor industries. The extremely low power CF-PCM *via* filament-induced heating can be utilized for the core memory of low-power and portable electronic applications.[7,16,21,36,37]

TEM and EDS Analyses. To clearly demonstrate the phase-change behavior of the CF-PCM, TEM analyses were performed. TEM samples directly obtained from the device successfully confirmed by the electrical measurements in Figure 2 were prepared by using a focused ion beam (FIB). Figure 4a shows the TEM images from the initial state of the CF-PCM device without the forming process. Clearly, no filaments were observed in the amorphous NiO layer located between the Ni (BE) and GST (Supporting Information, Figure S10). The initial GST films were polycrystalline structures, as determined through TEM observation and the selected area electron diffraction (SAED) pattern, because the annealing process under N_2 gas (at 473 K for 10 min) was performed after the CF-PCM device fabrication (Supporting Information, Figure S11).[8,14] Once an electric stress (CC = 1 mA) for electroforming was applied to the cell, a cone-shaped Ni CF started to form by reciprocal migration of Ni and oxygen vacancies, and the following reset process induced Joule heating for amorphization of GST (Figure 4b). A magnified TEM image was obtained from the red dotted square marked in Figure 4b. The Ni CF was confirmed as the polycrystalline phase through the fast Fourier transformed (FFT) pattern, corresponding to previously reported results.[31] The GST region contacted with the Ni CF was measured to be sub-10 nm in diameter and was changed to the amorphous state, whose FFT pattern also indicated an amorphous phase under the applied reset pulse. The contact area between the Ni filament and GST can be reduced to 1−2 nm with decreasing the CC for the electroforming process (Supporting Information, Figure S12a). Figure 4c shows TEM images from the device after the set process for recrystallization of GST, *i.e.*, transition of the contact area from the amorphous phase to the polycrystalline state. In addition, the Ni CF and GST films were verified from the EDS elemental mapping results, as shown in Figure 4d−g. Additional TEM/EDS images in Figures S12−14 also provide consistent results.

CONCLUSIONS

In summary, we introduced an innovative and scalable approach where a nanoscale Ni filament heater can significantly decrease the programming current of GST-based CF-PCM devices. The conventional resistor-type heater patterned by photolithography requires a complex and costly process for reducing the writing current. In contrast, our methodology can surpass the lithographic limit, self-forming the contact area between the filament and GST films below sub-10 nm. This nanoscale CF heater originating from filament-type resistive memories can transfer strong heat to phase-transition materials. The results reported in this study suggest that this approach provides a powerful solution for resolving the nanoscaling issue of PCRAM as a core memory in ultra-low-power electronics.

METHODS

CF-PCM Device Fabrication. Si substrates with 150 nm thick SiO_2 by dry oxidation were prepared, following deposition of a 20 nm thick Cr adhesion layer and a 250 nm thick Ni film using radio frequency (RF) sputtering. For the NiO formation (20 nm), Ni films were oxidized by using a reactive ion etching (RIE) system (power = 200 W, pressure = 10 mTorr, O_2 flow = 10 sccm, and time = 900 s). For the device fabrication of Figure 1, a Pt-coated probe tip (diameter of end point = 15 μm) was contacted onto the NiO films, applying voltage bias for filament formation. GST films (250 nm) and TiW TE (100 nm) were successively deposited and patterned. For the devices of Figure 2, all processes were equal to the CF-PCM device of Figure 1, except for the absence of filament formation *via* the Pt probe tip. For the CF-PCM device with a single Ni filament heater of Figure 3, the NiO oxidation time was changed from 900 s to 300 s for optimization of the filament-forming process. A Pt-coated CAFM tip (diameter of end point = 20 nm) was contacted onto the NiO films, sweeping the voltage from 0 to 10 V (CC = 10 μA). After the single Ni filament growth, the TiW/GST (100 nm/250 nm) was deposited and patterned.

Electrothermal Simulations. COMSOL multiphysics software (ALTSOFT) was used for the simulation modeling of phase-change behaviors in memory devices. The physical model defined by the electrothermal method was computed from the following equations. The mathematical model for heat transfer is the heat equation

$$\rho C \frac{\partial T}{\partial t} - \nabla(k\Delta T) = Q \quad (1)$$

where ρ is the density, T is the temperature, C is the heat capacity, k is the thermal conductivity, t is the time, and Q is the heat flux. The heat generated by Joule heating Q is given by

$$Q = \frac{1}{\sigma}|J|^2 = \sigma|\nabla V|^2 \quad (2)$$

where σ is the electric conductivity and J is the electric current density. The temperature distributions were numerically obtained from current density on the TE surface.

Electrical Measurements. Electrical characterizations and performance of the CF-PCM cells were measured by using a Keithley 4200-SCS (dc voltage/current sweep), a Keithley 4225-PMU (pulse generator and waveform capture of voltage/current), and a 4225-RPM (remote amplifier/switches). The resistance of the amorphous/crystalline states was caculated at a reading voltage of 0.3 V in all CF-PCM devices.

CAFM Measurements. The scanning of surface topography and current onto NiO films was executed with a scanning probe microscope (SPM), XE-100 model contact mode (Park Systems). The end point of the Pt-coated AFM tip has a diameter of 20 nm. The scan rate is 0.4 Hz and the tip bias is 0.5 V for the current scanning.

TEM/EDS Analyses. All samples for TEM observations were extracted from CF-PCM cells by using a dual-beam FIB (FEI NOVA 200) and ion milling with Ar ions. TEM and EDS analyses were executed with a JEOL JEM-ARM 200F microscope (200 kV) and a Bruker QUANTAX 400 EDS, respectievly.

Conflict of Interest: The authors declare no competing financial interest.

Acknowledgment. This work was financially supported by National Research Foundation (NRF) of Korea (NRF-2014R1A2A1A12067558) and the Center for Integrated Smart Sensors as Global Frontier Project (CISS-2012M3A6A6054193) funded by the Ministry of Science, ICT & Future Planning (MSIP), through NRF of Korea.

Supporting Information Available: The Supporting Information is available free of charge on the ACS Publications website at DOI: 10.1021/acsnano.5b02579.

REFERENCES AND NOTES

1. Wuttig, M. Phase-Change Materials: Towards a Universal Memory? *Nat. Mater.* **2005**, *4*, 265–266.
2. Raoux, S.; Burr, G. W.; Breitwisch, M. J.; Rettner, C. T.; Chen, Y. C.; Shelby, R. M.; Salinga, M.; Krebs, D.; Chen, S. H.; Lung, H. L.; *et al*. Phase-Change Random Access Memory: A Scalable Technology. *IBM J. Res. Dev.* **2008**, *52*, 465–479.
3. Lee, S. H.; Jung, Y.; Agarwal, R. Highly Scalable Non-Volatile and Ultra-Low-Power Phase-Change Nanowire Memory. *Nat. Nanotechnol.* **2007**, *2*, 626–630.
4. Lankhorst, M. H. R.; Ketelaars, B. W. S. M. M.; Wolters, R. A. M. Low-Cost and Nanoscale Non-Volatile Memory Concept for Future Silicon Chips. *Nat. Mater.* **2005**, *4*, 347–352.
5. Hamann, H. F.; O'Boyle, M.; Martin, Y. C.; Rooks, M.; Wickramasinghe, K. Ultra-High-Density Phase-Change Storage and Memory. *Nat. Mater.* **2006**, *5*, 383–387.
6. Wuttig, M.; Yamada, N. Phase-Change Materials for Rewriteable Data Storage. *Nat. Mater.* **2007**, *6*, 824–832.
7. Xiong, F.; Liao, A. D.; Estrada, D.; Pop, E. Low-Power Switching of Phase-Change Materials with Carbon Nanotube Electrodes. *Science* **2011**, *332*, 568–570.
8. Lencer, D.; Salinga, M.; Wuttig, M. Design Rules for Phase-Change Materials in Data Storage Applications. *Adv. Mater.* **2011**, *23*, 2030–2058.
9. Wong, H. S. P.; Raoux, S.; Kim, S.; Liang, J. L.; Reifenberg, J. P.; Rajendran, B.; Asheghi, M.; Goodson, K. E. Phase Change Memory. *Proc. IEEE* **2010**, *98*, 2201–2227.
10. Zhang, W.; Thiess, A.; Zalden, P.; Zeller, R.; Dederichs, P. H.; Raty, J. Y.; Wuttig, M.; Blugel, S.; Mazzarello, R. Role of Vacancies in Metal-Insulator Transitions of Crystalline Phase-Change Materials. *Nat. Mater.* **2012**, *11*, 952–956.
11. Loke, D.; Lee, T. H.; Wang, W. J.; Shi, L. P.; Zhao, R.; Yeo, Y. C.; Chong, T. C.; Elliott, S. R. Breaking the Speed Limits of Phase-Change Memory. *Science* **2012**, *336*, 1566–1569.
12. Nam, S. W.; Chung, H. S.; Lo, Y. C.; Qi, L.; Li, J.; Lu, Y.; Johnson, A. T. C.; Jung, Y. W.; Nukala, P.; Agarwal, R. Electrical Wind Force-Driven and Dislocation-Templated Amorphization in Phase-Change Nanowires. *Science* **2012**, *336*, 1561–1566.
13. Atwood, G. Phase-Change Materials for Electronic Memories. *Science* **2008**, *321*, 210–211.
14. Zhu, M.; Xia, M.; Rao, F.; Li, X.; Wu, L.; Ji, X.; Lv, S.; Song, Z.; Feng, S.; Sun, H.; *et al*. One Order of Magnitude Faster Phase Change at Reduced Power in Ti-Sb-Te. *Nat. Commun.* **2014**, *5*, 4086.
15. Pandian, R.; Kooi, B. J.; Palasantzas, G.; De Hosson, J. T. M.; Pauza, A. Nanoscale Electrolytic Switching in Phase-Change Chalcogenide Films. *Adv. Mater.* **2007**, *19*, 4431–4437.
16. Park, W. I.; You, B. K.; Mun, B. H.; Seo, H. K.; Lee, J. Y.; Hosaka, S.; Yin, Y.; Ross, C. A.; Lee, K. J.; Jung, Y. S. Self-Assembled Incorporation of Modulated Block Copolymer Nanostructures in Phase-Change Memory for Switching Power Reduction. *ACS Nano* **2013**, *7*, 2651–2658.
17. Jeyasingh, R.; Fong, S. W.; Lee, J.; Li, Z. J.; Chang, K. W.; Mantegazza, D.; Asheghi, M.; Goodson, K. E.; Wong, H. S. P. Ultrafast Characterization of Phase-Change Material Crystallization Properties in the Melt-Quenched Amorphous Phase. *Nano Lett.* **2014**, *14*, 3419–3426.
18. Orava, J.; Greer, A. L.; Gholipour, B.; Hewak, D. W.; Smith, C. E. Characterization of Supercooled Liquid $Ge_2Sb_2Te_5$ and Its Crystallization by Ultrafast-Heating Calorimetry. *Nat. Mater.* **2012**, *11*, 279–283.
19. Choi, Y.; Song, I.; Park, M.-H.; Chung, H.; Chang, S.; Cho, B.; Kim, J.; Oh, Y.; Kwon, D.; Sunwoo, J.; *et al*. A 20nm 1.8V 8Gb PRAM with 40MB/s Program Bandwidth. *ISSCC Dig. Technol. Pap.* **2012**, 46–48.
20. Simpson, R. E.; Fons, P.; Kolobov, A. V.; Fukaya, T.; Krbal, M.; Yagi, T.; Tominaga, J. Interfacial Phase-Change Memory. *Nat. Nanotechnol.* **2011**, *6*, 501–505.
21. Xiong, F.; Bae, M. H.; Dai, Y.; Liao, A. D.; Behnam, A.; Carrion, E. A.; Hong, S.; Ielmini, D.; Pop, E. Self-Aligned Nanotube-Nanowire Phase Change Memory. *Nano Lett.* **2013**, *13*, 464–469.
22. Lee, M. J.; Lee, C. B.; Lee, D.; Lee, S. R.; Chang, M.; Hur, J. H.; Kim, Y. B.; Kim, C. J.; Seo, D. H.; Seo, S.; *et al*. A Fast, High-Endurance and Scalable Non-Volatile Memory Device Made from Asymmetric Ta_2O_{5-x}/TaO_{2-x} Bilayer Structures. *Nat. Mater.* **2011**, *10*, 625–630.
23. Harriott, L. R. Limits of Lithography. *Proc. IEEE* **2001**, *89*, 366–374.
24. Jung, Y.; Lee, S. H.; Jennings, A. T.; Agarwal, R. Core-Shell Heterostructured Phase Change Nanowire Multistate Memory. *Nano Lett.* **2008**, *8*, 2056–2062.
25. Lee, S. H.; Jung, Y. W.; Agarwal, R. Size-Dependent Surface-Induced Heterogeneous Nucleation Driven Phase-Change in $Ge_2Sb_2Te_5$ Nanowires. *Nano Lett.* **2008**, *8*, 3303–3309.
26. Jung, Y.; Yang, C. Y.; Lee, S. H.; Agarwal, R. Phase-Change Ge-Sb Nanowires: Synthesis, Memory Switching, and Phase-Instability. *Nano Lett.* **2009**, *9*, 2103–2108.
27. Han, N.; Kim, S. I.; Yang, J. D.; Lee, K.; Sohn, H.; So, H. M.; Ahn, C. W.; Yoo, K. H. Phase-Change Memory in Bi_2Te_3 Nanowires. *Adv. Mater.* **2011**, *23*, 1871–1875.
28. Sawa, A. Resistive Switching in Transition Metal Oxides. *Mater. Today* **2008**, *11*, 28–36.
29. Wong, H. S. P.; Lee, H. Y.; Yu, S. M.; Chen, Y. S.; Wu, Y.; Chen, P. S.; Lee, B.; Chen, F. T.; Tsai, M. J. Metal-Oxide RRAM. *Proc. IEEE* **2012**, *100*, 1951–1970.
30. Waser, R.; Dittmann, R.; Staikov, G.; Szot, K. Redox-Based Resistive Switching Memories - Nanoionic Mechanisms, Prospects, and Challenges. *Adv. Mater.* **2009**, *21*, 2632–2663.
31. You, B. K.; Park, W. I.; Kim, J. M.; Park, K. I.; Seo, H. K.; Lee, J. Y.; Jung, Y. S.; Lee, K. J. Reliable Control of Filament Formation in Resistive Memories by Self-Assembled Nanoinsulators Derived from a Block Copolymer. *ACS Nano* **2014**, *8*, 9492–9502.
32. Lee, M. J.; Han, S.; Jeon, S. H.; Park, B. H.; Kang, B. S.; Ahn, S. E.; Kim, K. H.; Lee, C. B.; Kim, C. J.; Yoo, I. K.; *et al*. Electrical Manipulation of Nanofilaments in Transition-Metal Oxides for Resistance-Based Memory. *Nano Lett.* **2009**, *9*, 1476–1481.
33. Yoon, J. H.; Han, J. H.; Jung, J. S.; Jeon, W.; Kim, G. H.; Song, S. J.; Seok, J. Y.; Yoon, K. J.; Lee, M. H.; Hwang, C. S. Highly Improved Uniformity in the Resistive Switching Parameters of TiO_2 Thin Films by Inserting Ru Nanodots. *Adv. Mater.* **2013**, *25*, 1987–1992.
34. Lacaita, A. L. Phase Change Memories: State-of-the-Art, Challenges and Perspectives. *Solid-State Electron.* **2006**, *50*, 24–31.
35. Jeong, D. S.; Thomas, R.; Katiyar, R. S.; Scott, J. F.; Kohlstedt, H.; Petraru, A.; Hwang, C. S. Emerging Memories: Resistive Switching Mechanisms and Current Status. *Rep. Prog. Phys.* **2012**, *75*, 076502.
36. Kim, S.; Son, J. H.; Lee, S. H.; You, B. K.; Park, K. I.; Lee, H. K.; Byun, M.; Lee, K. J. Flexible Crossbar-Structured Resistive Memory Arrays on Plastic Substrates *via* Inorganic-Based Laser Lift-Off. *Adv. Mater.* **2014**, *26*, 7480–7487.
37. Mondal, S.; Chueh, C. H.; Pan, T. M. High-Performance Flexible Ni/Sm_2O_3/ITO ReRAM Device for Low-Power Non-volatile Memory Applications. *IEEE Electron Device Lett.* **2013**, *34*, 1145–1147.